Progress In Electromagnetics Research B, Vol. 95, 141–162, 2022

Time-reversal of Sub-THz Pulses in Complex Media

Ali Mokh[1], Ramin Khayatzadeh[2], Abdelwaheb Ourir[1], Mohamed Kamoun[2], Arnaud Tourin[1], Mathias Fink[1], and Julien de Rosny[1, *]

Abstract—For the last 20 years, the time-reversal (TR) process has been successfully applied to focus pulses in the microwave frequency range and in complex media. Here we examine the specific conditions to obtain the same results but in the sub-THz frequency range. Because of the stronger attenuation at this much higher frequency, it is more challenging to exploit the TR self-focusing property. The TR of pulses is studied in two kinds of complex media: metallic waveguide and leaky reverberating cavity. For each medium, we propose one or two models to assess the quality of the focusing. For the waveguide, we show that the angle of incidence is an important parameter. Based on these results, we perform TR experiments at 273 GHz with a bandwidth that can be as large as 2 GHz. TR experiments are successfully first conducted in a 1 m long and 10 mm diameter straight hollow cylinder and then in a 5 m long and 12 mm diameter curved waveguide. Finally, we present results obtained in a cavity of 72 cm^3 that leaks through a copper grid. The best focusing is observed with the longer waveguide.

1. INTRODUCTION

The terahertz radiofrequency domain ranges between millimeter and infrared waves. This frequency spectrum is unique because it combines two interesting features: a resolution that can be as small as a tenth of a millimeter, and many different dry materials are transparent to them. However, this frequency range lies in the THz gap, in other words, the frequency range that is too high for conventional semiconductor technology and too low for optical devices based on electronic transitions. Therefore, only a limited number of teams, mainly devoted to radio astronomy, worked on the THz applications up to the 90 s. Then a dramatic change occurred after the introduction of the time domain spectroscopy (TDS), which greatly accelerates THz studies. Thus, many fields now employ THz radiation: medical imaging, security scanners, non-destructive testing, and high rate telecommunications. Referring to [1], industrial developments between 300 GHz and 500 GHz are the most realistic because of the recent progress in semiconductor devices and circuits. According to the International Technology Roadmap for Semiconductors (ITRS), the cut-off frequency of Si-CMOS will exceed 500 GHz within a few years. At the THz spectrum low-end (between 100 GHz and 1 THz), when using broadband sources, THz studies in the time domain share many aspects with ultrasonic studies. Indeed, the acoustic wavelength at 1.5 MHz in water is equal to the THz wavelength at 300 GHz, and probing devices for both kinds of waves give access to the transient field. Therefore, ultrasonic application areas are very similar to those of THz.

Thirty years ago, based on the time-reversal symmetry of ultrasonic waves and because of the progress of fast analog to digital and digital to analog converters, a new device, so-called time-reversal mirror, has been proposed to focus ultrasonic waves [2, 3]. A time-reversal mirror is made of an array of transceivers that probes the time dependence of an incident wave field in a first step and plays

Received 4 February 2022, Accepted 8 April 2022, Scheduled 22 May 2022
* Corresponding author: Julien de Rosny (julien.derosny@espci.fr).
[1] Institut Langevin, ESPCI Paris, Université PSL, CNRS, Paris 75005, France. [2] Mathematical and Algorithmic Science Lab, France Research Center, Huawei Technologies Co., Ltd., France.

back the recorded signals, but in reverse order, in a second step. Initially developed to compensate for wavefront distortion due to weak aberrating media, it has rapidly shown its efficiency in rich multipath environments. This effect was first observed in strong multiple scattering media [4], and then in waveguides [5]. Indeed, in a complex environment, the TR process undoes the multipath and maximizes the signal strength at the focus. A strong spatio-temporal focus was obtained with a single transceiver in reverberating cavities [6]. A few years later, the concept has been applied to the UHF band [7, 8]. The TR self-focusing property has been successfully used in several applications such as wireless communications [9], source localization [10], medical therapy [11, 12], non-destructive testing [13, 14], and general imaging [15].

Similar applications are also actively studied with THz radiation, for example, cancer therapy [16], cell stimulation [17], security screening [18], quality control [19], and communications [20]. Thus, like for ultrasonic applications, time-reversal may be relevant to improving some of these THz applications.

In the THz range, Time Reversal principle has been mainly applied for imaging. Time reversal imaging belongs to the wideband numerical holographic methods [21]. Indeed, TR imaging consists of an algorithm based on the TR symmetry of the Maxwell equations to numerically back-propagate a pulsed field probed by a TDS on a plane toward a diffraction area. It was first applied to 2D imaging [22, 23] and later 3D reflection imaging [24]. It was also used to inspect dielectric structures [25]. Similar to the ultrasonic waveguide used in [5] which induced a smaller focal spot, an electromagnetic waveguide was utilized in [26] to improve the image resolution.

Here our aim is to take the benefit of the TR in complex media to focus spatially and temporally a sub-THz burst using a single emitter. In particular, we expect that TR can overcome a central issue facing the THz community by effectively collecting energy that is dispersed in rich multipath environments.

To that end, we propose to study the focusing properties of time-reversed waves at 273.6 GHz and with a bandwidth up to 2 GHz in two kinds of multipath media: waveguide and leaking reverberation cavity. We begin by quantifying the focusing performances of TR in the particular case of relative small bandwidth and strong attenuation either using analytical or numerical models. Then we experimentally validate these approaches on three configurations based on a solid state modulator and a solid state demodulator.

The paper is organized as follows. In Section 2, we propose a brief general introduction to the principle of time-reversal. We focus on the baseband TR and pulse compression techniques to improve the signal-to-noise ratio. Section 3 presents a heuristic model based on the image theorem to intuitively explain the focusing property in waveguides. However, this model is inaccurate for circular waveguides. Therefore, we introduce a model based on the modal decomposition of the wavefield. The last part of this section presents a model based on shot-noise for the leaky cavity. Because no analytical expression can be derived for the modal modeling of the waveguide, we propose to numerically evaluate the focusing property in a circular waveguide with respect to the angle of incidence and the bandwidth. Section 4 presents the transmitting and receiving devices used in the experiment, and the setup is detailed. Experimental results obtained at 273 GHz are presented in Section 5. These results have been obtained in two different waveguides (1 m-long straight and 5 m long curved waveguides) and one leaky cavity. Based on these results, the last part is devoted to the applicability of TR in the sub-THz range.

2. TIME-REVERSAL PROCESSING

A time reversal process is composed of 2 steps (see Fig. 1). In the first step (see Fig. 1(a)), an antenna A at position $\mathbf{r}_A$ emits a baseband signal $e(t)$, and the signal $s(t)$ received on an antenna B at position $\mathbf{r}_B$ can be written in terms of the complex impulse response (CIR) $h_{AB}(\mathbf{r}_A, \mathbf{r}_B; t)$ between antennas A and B

$$s(t) = h_{AB}(\mathbf{r}_A, \mathbf{r}_B; t) * e(t), \tag{1}$$

where symbol $*$ stands for the time convolution operator. In the second step, the signal $s(t)$ is flipped in time and reemitted by antenna B (see Figs. 1(c) and (d)). The signal received on antenna A, which is now at position $\mathbf{r}'_A$, is therefore given by

$$\begin{aligned} y(\mathbf{r}_A, \mathbf{r}'_A; t) &= s^*(-t) * h_{BA}(\mathbf{r}_B, \mathbf{r}'_A; t), \\ &= e^*(-t) * h^*_{AB}(\mathbf{r}_A, \mathbf{r}_B; -t) * h_{BA}(\mathbf{r}_B, \mathbf{r}'_A; t). \end{aligned} \tag{2}$$

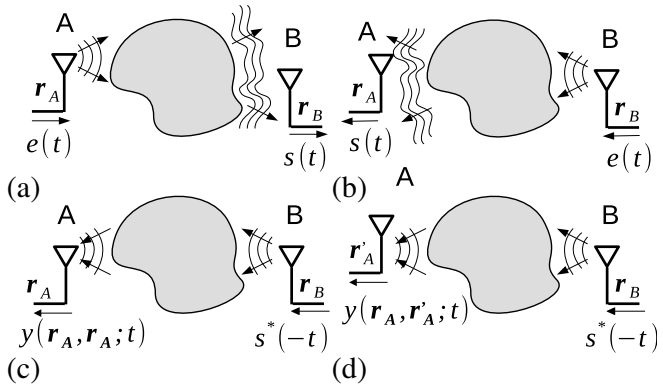

Figure 1. Principle of Time Reversal processing. In (a) a signal $e(t)$ is emitted by an antenna A at position $\mathbf{r}_A$ toward a complex media represented by the gray area. The signal $s(t)$ resulting from the wavefield propagation through the complex media is recorded by an antenna B at position $\mathbf{r}_B$. Thanks to the reciprocity of the medium, the same signal $s(t)$ is recorded on antenna A when antenna B emits $e(t)$. In (c) and (d), the signal $s(t)$ flipped in time is sent back by antenna B. Note that the radiation pattern of the reemitted field before interacting with the complex media corresponds to the one of the single antenna B (e.g., omnidirectional). The focused signal is recorded (a) either at the initial position $\mathbf{r}_A$ or (b) at another position $\mathbf{r}'_A$ to probe the focal spot.

Note that in a reciprocal media if the signal $e(t)$ is transmitted by antenna B instead of antenna A during the first step of time reversal, the same signal $s(t)$ is obtained on antenna A because $h_{AB}(\mathbf{r}_A, \mathbf{r}_B; t) = h_{BA}(\mathbf{r}_B, \mathbf{r}_A; t)$ (see Figs. 1(a) and (b)). In the following we are going to use this reciprocity mode that does not require to switch the source and the receiver role between the 2 steps of TR.

It is useful to rewrite $y(\mathbf{r}_A, \mathbf{r}'_A; t)$ in terms of the correlation function $R_{hh'}(t)$,

$$y(\mathbf{r}_A, \mathbf{r}'_A; t) = e^*(-t) * R_{hh'}(t), \tag{3}$$

where the expression of the correlation is

$$R_{hh'}(t) = h^*_{BA}(\mathbf{r}_B, \mathbf{r}_A; -t) * h_{BA}(\mathbf{r}_B, \mathbf{r}'_A; t), \tag{4}$$

The real (respectively imaginary) part of this correlation function is symmetric (respectively asymmetric) with respect to time $t = 0$ when $\mathbf{r}'_A = \mathbf{r}_A$. In a complex media, $h_{BA}(\mathbf{r}_B, \mathbf{r}_A; t)$ is random in time and leads to a peaked correlation function when $\mathbf{r}'_A = \mathbf{r}_A$. In other words, in complex media, the time reversed field $y(\mathbf{r}_A, \mathbf{r}'_A; t)$ focuses in space and in time. Note that the focusing occurs at $t = 0$ because, in this instance, for simplicity, we do not consider the time delay between the recording step and transmission step by the TR element. An important effect of this TR focusing in a complex media is the enhancement of the TR field compared to the one obtained without TR processing. This enhancement effect arises when considering that all the signals are transmitted with the same maximum amplitude that is a feature of the generator (see Appendix D.1 for a demonstration).

Of course the CIR results from all the electric and electromagnetic effects. Thus, the effect of polarization is included into $h_{BA}(\mathbf{r}_B, \mathbf{r}_A; t)$. For instance, in the case of linearly polarized dipole antenna B, $h_{BA}(\mathbf{r}_B, \mathbf{r}_A; t)$ can be approximated by

$$h_{BA}(\mathbf{r}_B, \mathbf{r}_A; t) \propto \mathbf{p}^t_A \mathbf{E}_B \tag{5}$$

where $\mathbf{p}_A$ is the polarization direction of the dipole A, and $\mathbf{E}_B$ is the electric field generated at the position $\mathbf{r}_A$ by the antenna B. Subscript ^{t} corresponds to the transpose operator, and therefore $\mathbf{p}^t_A \mathbf{E}_B$ can be interpreted as the scalar product between vectors $\mathbf{p}_A$ and $\mathbf{E}_B$.

Usually, for ultrasonic applications, for instance, the emitted signal $e(t)$ is a short pulse with a duration typically of the order of the inverse of the system bandwidth. However, with such a signal, the THz radiated energy is not sufficient to probe the channel because the signal-to-noise ratio (SNR) of THz transmission is very low. To overcome this issue, instead of a pulse, a linear frequency modulated

(LFM) waveform $e_{FM}(t)$ can be used to take the benefit of the pulse compression effect. To lower secondary lobes, before emission a Hanning window apodizes the signal $e_{FM}(t)$. Instead of directly flipping in time the signal $s(t)$, an estimation of the impulse response $\tilde{h}_{BA}(\mathbf{r}_B, \mathbf{r}_A; t)$ within the working bandwidth is obtained by correlating $s(t)$ with $e_{FM}(t)$, i.e.,

$$\tilde{h}_{BA}(\mathbf{r}_B, \mathbf{r}_A; t) = s(t) * e^*_{FM}(-t). \tag{6}$$

Then this estimation is flipped in time, in other words, $\tilde{h}_{BA}(\mathbf{r}_B, \mathbf{r}_A; t) \rightarrow \tilde{h}^*_{BA}(\mathbf{r}_B, \mathbf{r}_A; -t)$. For the same SNR issue, before emission, $\tilde{h}^*_{BA}(\mathbf{r}_B, \mathbf{r}_A; -t)$ is convolved with $e_{FM}(t)$. The same pulse compression technique is applied to the received signal $s_{TR}(t)$ to extract the time-reversed signal $y(t)$,

$$y(\mathbf{r}_A, \mathbf{r}'_A; t) = s_{TR}(t) * e^*_{FM}(-t). \tag{7}$$

One drawback of this technique is that TR does not anymore induce an amplitude enhancement because the LFM is much longer than the CIR. Nevertheless, we still take the benefit of the spatio-temporal focusing. To quantify the quality of the focusing, we introduce the signal to interference ratio (SIR) which is given by the ratio of the squared value of the peak level at the focus over the squared maximum values sampled out of the focus, i.e.,

$$\mathrm{SIR} = \frac{|y(\mathbf{r}_A, \mathbf{r}_A; 0)|^2}{\dfrac{1}{N_{\mathbf{r}_{A'}} - 1} \displaystyle\sum_{\mathbf{r}_{A'} \neq \mathbf{r}_A} \max_t |y(\mathbf{r}_A, \mathbf{r}_{A'}; t)|^2} \tag{8}$$

where $N_{\mathbf{r}_{A'}}$ is the number of scanning positions of the TR field including at the focus ($\mathbf{r}_{A'} = \mathbf{r}_A$).

3. MODELS

3.1. Straight Waveguide

A waveguide is a complex media where waves can undergo many reflections off the boundaries. Twenty years ago, it was shown that a time-reversal mirror can very efficiently unravel all the paths and generate a strong focused pulse. This property has been observed experimentally in a 1 m long ultrasonic waveguide in a water tank [5] at a working frequency of 1 MHz. Simultaneously, the same focusing effect at a few kHz has been reported on a large-scale experiment performed in the Mediterranean Sea [9].

The main difficulty for transposing these experiments in the THz electromagnetic spectrum is the much smaller relative bandwidth. Indeed, in the aforementioned works, the relative bandwidth lies between 14% and 50%, while it is smaller than 4% in our case. This constraint drastically reduces the time spreading of the CIR. Indeed, when using an omnidirectional TR antenna, the transmitted field is dominated by the paths undergoing only a few reflections off the waveguide boundaries. Because the travel times of these paths are very similar, the time dispersion is limited. To overcome this issue, we propose to time reverse the field with a directive antenna illuminating the waveguide with an important angle of incidence. In such a configuration, the field is forced to be reflected many times between the 2 waveguide extremities.

We first validate qualitatively this approach with a ray-based model and then quantitatively with a modal based model.

3.1.1. Ray Model

Our ray-like model is based on the principle of mirror images, which assumes a rectangular cross-section waveguide. This model has been proposed previously for the interpretation of TR focusing observed in an acoustic waveguide [5]. As shown in Fig. 2, the image theorem consists of replacing the effect of the waveguide walls with virtual sources. Hence compared to free space, the improvement of TR focusing is related to virtual TR elements that increase the total aperture of the TR mirror. Based on geometrical considerations, we start by estimating the dispersion ΔT of the CIR.

The length and width of the 2D waveguide shown in Fig. 2 are equal to L and d, respectively. The aperture angle of the emitting horn antenna is δ. The inclination angle of the transmitting antenna with

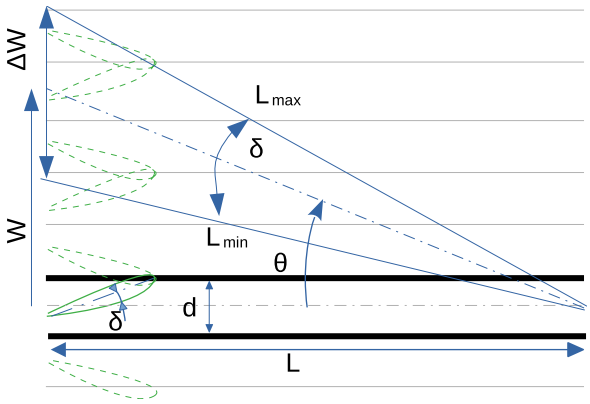

Figure 2. An illustration of the application of the image theorem. The two thick horizontal lines represent the waveguide metallic walls. The thin horizontal lines are the walls' images. On the left, the thick green radiation pattern represents the main lobe of the Tx antenna. The dashed green line patterns are the images of the TR element with respect to the wall images.

respect to the waveguide axis is θ. Due to their directivity, the incident angle of the virtual antenna, which mainly contributes to the signal on the omnidirectional Rx antenna, is between $\theta-\delta/2$ and $\theta+\delta/2$ (see Fig. 2). From the difference between the minimum and maximum optical path lengths ($L_{\min}$ and $L_{\max}$ on Fig. 2), it can be shown that under the assumption that $\delta \ll \theta$, ΔT is

$$\Delta T = \frac{4L\,|\sin(\theta)|\,\delta}{c\cos^2(\theta)}. \tag{9}$$

For instance, for a 1 m long waveguide with the directivity of the experimental horns (see experimental section), the bandwidth should be at least larger than 500 MHz when θ equals 60°.

Another important parameter is the number of echoes within the time ΔT. For a 2D waveguide, as shown in Fig. 2, the number of contributing virtual TR elements is given by the width of the beam ΔW at the distance L from the source divided by twice the height of the waveguide d (see Fig. 2). The factor 2 comes from the fact that only half of the virtual beams are oriented toward the receiver. As a consequence, the number of virtual sources is given by

$$N_{2D} = \frac{2L}{d}\left(\frac{2}{\cos(\theta)^2} - 1\right)\delta. \tag{10}$$

For a 3D waveguide with a rectangular cross-section, the time dispersion is the same but the number of contributing elements is now given by $2\pi\Delta WW/4d^2$ which is proportional to the surface of a ring of thickness ΔW and radius W. The factor 1/4 originates the fact that only a quarter of the images are pointing toward the Rx antenna. We deduce the expression of the number of virtual sources,

$$N_{3\mathrm{D}} = \frac{L^2\tan(\theta)}{d^2}\left(\frac{2}{\cos(\theta)^2} - 1\right)\delta. \tag{11}$$

Eq. (9) and either Eq. (10) or Eq. (11) depending on the 2D or 3D waveguide dimension show that a larger incidence angle θ allows to simultaneously increase the number of virtual sources and the pulse dispersion. Because of the Taylor expansion with respect to δ, ΔT, $N_{2\mathrm{D}}$ and $N_{3\mathrm{D}}$ linearly depend on it. Hence, on one side, a too small aperture angle would make useless the effect of a large incident angle. But on the other side, as explained, in case of a too large aperture angle, the transmission would be dominated by the few paths with a limited number of reflections leading to a small number of effective images contributing to the focusing. Therefore, the choice of aperture angle is a matter of compromise.

Finally, assuming that a sufficiently large number of virtual sources are involved in generating a good time reversed field, the focusing is intrinsically limited by the diffraction. Because the angular aperture of the virtual array of sources is equal to δ, the width of the focal spot equals λ/δ.

Considering a 10 mm width squared section waveguide, an incident angle of 60° and an aperture angle of 10°, the number of virtual sources is 87 at 2D and about 11000 at 3D. In fact, this very high

number of virtual sources shows the limit of the ray-like model because, as we demonstrate in the modal analysis of TR, it is larger than the number of excited modes. Nevertheless, this ray approach provides an intuitive way to understand the interest of the inclination of the Tx horn antenna to increase the wave dispersion.

3.1.2. Modal Model

The steps to compute the TR field are shown in Fig. 3. In a waveguide, any field can be advantageously decomposed over propagating modes. There are two families of propagating modes: the transverse electric (TE) and transverse magnetic (TM) modes. For a waveguide of axis $\hat{\mathbf{z}}$ and a source B generating an electric field $\bar{\mathbf{E}}_B(x,y,z)$ at $z=0$, the field at positions A ($\mathbf{r}_A=(x_A,y_A,z_A)$) is written as

$$\bar{\mathbf{E}}(\mathbf{r}_A)=\sum_{m=0,\nu=0,n=1}^{1,\infty,\infty}\left\langle \mathscr{E}^m_{\nu,n}(x,y)\right|\left.\bar{\mathbf{E}}_B(x,y,z=0)\right\rangle\times\mathscr{E}^m_{\nu,n}(x_A,y_A)e^{\left(-j\beta^m_{\nu,n}-\frac{\alpha^m_{\nu,n}}{2}\right)z_A}. \tag{12}$$

$\bar{\mathbf{E}}(\mathbf{r}_A)$ stands for the Fourier transform of $\mathbf{E}(\mathbf{r}_A;t)$. For conciseness, the frequency dependence of $\bar{\mathbf{E}}(\mathbf{r}_A)$ is implicit. The expression of the Hilbert inner-product is

$$\langle\mathbf{f}(x,y)|\,\mathbf{g}(x,y)\rangle=\sum_{i=x,y,z}\int_S f_i^*(x,y)g_i(x,y)dxdy \tag{13}$$

where $\mathscr{E}^0_{\nu,n}(x,y)$ and $\mathscr{E}^1_{\nu,n}(x,y)$ are the electric field components of the TE and TH eigen-modes, respectively. The longitudinal wavenumber $\beta^m_{\nu,n}$ is deduced from the discrete set of transverse wavenumbers $k^m_{\nu,n}$ associated with each mode. Indeed,

$$\beta^m_{\nu,n}=k_0^2-(k^m_{\nu,n})^2,$$

where k_0 is the wavenumber. The damping factor $e^{-\alpha^m_{\nu,n}z}$ is due to ohmic losses. The attenuation coefficient $\alpha^m_{\nu,n}$ depends on the mode cut-off frequency, the waveguide radius, and the angular frequency. We assume that the source B generates a vertically polarized (parallel to axis $\hat{\mathbf{x}}$) beam of width a directed toward the direction $\mathbf{n}_{inc}$. The center of the beam on the cross-section $z=0$ is at position $\mathbf{r}_B$. The electric field $\mathbf{E}_B(x,y,z)$ at $z=0$ is approximated by

$$\bar{\mathbf{E}}_B(x,y,z=0)=e^{jk_0\mathbf{n}^t_{inc}(\mathbf{r}-\mathbf{r}_B)}o\left(\frac{\|\mathbf{r}-\mathbf{r}_B\|}{a}\right)\hat{\mathbf{x}}, \tag{14}$$

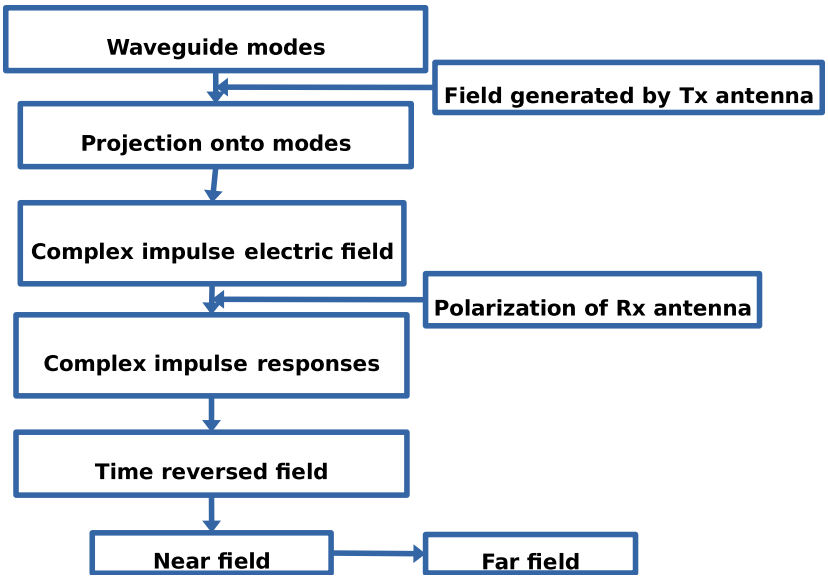

Figure 3. Schematic representation of the different steps to compute the time reversed field.

where $\mathbf{r} = x\hat{\mathbf{x}} + y\hat{\mathbf{y}}$ and o is an aperture function such as

$$o(\rho) = \begin{cases} \cos\left(\frac{\pi\rho}{2}\right) e^{-\left(\frac{\pi\rho}{2}\right)^2} & \text{when } \rho < 1 \\ 0 & \text{when } \rho > 1 \end{cases} \tag{15}$$

We first study the focusing at the waveguide extremity $z = L$. As explained in Section 2, the channel response between the source antenna and the dipole antenna at position $\mathbf{x}_A$ is given by (5). In the Fourier domain, the expression of correlation function (4) becomes

$$\bar{R}_{hh'} = \bar{h}^*_{BA}(\mathbf{r}_B, \mathbf{r}_A)\bar{h}_{BA}(\mathbf{r}_B, \mathbf{r}'_A). \tag{16}$$

As a consequence for a flat spectrum excitation signal $e(t)$ of bandwidth Δf, the baseband TR field at position $\mathbf{r}'_A$ and for a polarization $\mathbf{p}'_A$ is given by

$$y(\mathbf{r}_A, \mathbf{r}'_A, t) \propto \int_{-\pi\Delta f}^{\pi\Delta f} \left(\mathbf{p}'^t_A \bar{\mathbf{E}}_B(\mathbf{x}'_{A'})\right) \left(\mathbf{p}^t_A \cdot \bar{\mathbf{E}}^*_B(\mathbf{x}_A)\right) e^{-j\delta\omega t} d\delta\omega. \tag{17}$$

In practice, one may want to benefit from the TR to beam a pulse in the far field of the waveguide. For simplicity, we assume that the cylinder leads to a perfect electric conductor with a circular hole of the same diameter as the cylinder one. In such a case, the far-field electric field in direction $\hat{\mathbf{n}}_A$ is given by

$$\mathbf{E}^f_B(\hat{\mathbf{n}}_A) = -\frac{jk_0 e^{jk_0 R}}{4\pi R} \hat{\mathbf{n}}_A \times (\hat{\mathbf{z}} \times \mathbf{f}(\hat{\mathbf{n}}_A)), \tag{18}$$

where $\mathbf{f}$ is the Fourier transform of the electrical field at the aperture,

$$\mathbf{f}(\hat{\mathbf{n}}_A) = \int_S \mathbf{E}_B(x, y, z = L) e^{jk_0 \hat{\mathbf{n}}^t_A \mathbf{r}} dxdy. \tag{19}$$

Under the small angle approximation ($\mathbf{n}_{out} \approx \mathbf{z}$), the previous expression can be simplified into

$$\mathbf{E}^f(\hat{\mathbf{n}}_A) \approx \frac{jk_0 e^{jk_0 R}}{4\pi R} \mathbf{f}(\hat{\mathbf{n}}_A). \tag{20}$$

Based on the previous equation and (16), the far field time reversal is given by,

$$y(\mathbf{r}_A, \mathbf{r}'_A, t) \propto \int_{-\pi\Delta f}^{\pi\Delta f} \frac{1}{4\pi R} \left(\mathbf{p}^t_A \mathbf{f}(\hat{\mathbf{n}}'_A)\right) \left(\mathbf{p}^t_A \mathbf{f}^*(\hat{\mathbf{n}}_A)\right) e^{-j\delta\omega t} d\delta\omega, \tag{21}$$

where $\hat{\mathbf{n}}_A$ and $\hat{\mathbf{n}}'_A$ are the direction of the dipole antenna during the first step of TR process and the direction of observation of the time reversed wave during the second step. The model is evaluated numerically in Section 4.

3.2. Cavity

Contrary to waveguides, several models have been developed to describe the behavior of TR in a cavity. The most accurate model is based on a modal decomposition of the electromagnetic field inside the cavity [27]. However, as shown by Drager et al. [28], when the decay time is smaller than the modal density (Heisenberg time) of the cavity, the modes of the cavity strongly overlap, and the CIR can be represented by a shot noise model, also called Rayleigh fading. In such a case, the CIR is given by

$$h_{BA}(r, t = n/\Delta f) = \begin{cases} a'_n e^{-\frac{n}{\Delta f \tau}} & n \geq 0 \\ 0 & n < 0 \end{cases} \tag{22}$$

where Δf and τ are the bandwidth and reverberation time of the cavity. The coefficients a_n are uncorrelated, zero-mean, complex Gaussian variables, in other words,

$$\left\langle a'_n \right\rangle = 0, \tag{23}$$

$$\left\langle a'_n a'^*_m \right\rangle = A\delta_{nm}. \tag{24}$$

The notation $\langle\cdot\rangle$ stands for the statistical averaging. This model has also been introduced to describe the time-reversal focusing in multiple scattering media [29]. Using (4) and (22), the autocorrelation ($\mathbf{r}_A = \mathbf{r}'_A$) is written as

$$R_{hh}(t = n/\Delta f) = \sum_{k=\max(0,n)}^{\infty} a'_k a'^{*}_{k-n} e^{-\frac{k}{\Delta f \tau}} e^{n/2\tau} \tag{25}$$

One can show (see Appendix) that the SIR is then approximated by

$$\mathrm{SIR} = \frac{\Delta f \tau}{2}, \tag{26}$$

The spacial dependence of the focusing at $t = 0$ can be derived from

$$y(\mathbf{r}_A, \mathbf{r}'_A, t = 0) \propto \int_{-\pi\Delta f}^{\pi\Delta f} \bar{h}^{*}_{BA}(\mathbf{r}_B, \mathbf{r}_A) \bar{h}_{BA}(\mathbf{r}_B, \mathbf{r}'_A) d\delta\omega. \tag{27}$$

Indeed, it has been shown that the TR in random media is a self-averaging process [30], the integral over frequency can be replaced by an overage over disorder, i.e.,

$$y(\mathbf{r}_A, \mathbf{r}'_A, t = 0) \propto 2\pi\Delta f \left\langle \bar{h}^{*}_{BA}(\mathbf{r}_B, \mathbf{r}_A) \bar{h}_{BA}(\mathbf{r}_B, \mathbf{r}'_A) \right\rangle \tag{28}$$

Because one can approximate the leaking face of the cavity as an incoherent source, the statistical correlation between $\bar{h}_{BA}(\mathbf{r}_B, \mathbf{r}_A)$ and $\bar{h}_{BA}(\mathbf{r}_B, \mathbf{r}'_A)$ is well approximated by the Van Citter-Zernike theorem [31] which states that it is given by the 2D Fourier transform of the aperture. Assuming a rectangle leaking area of width W_x and height W_y and included in the plane defined by $z = 0$, the focal spot at the distance z_A is well approximated by

$$y(\mathbf{r}_A, \mathbf{r}'_A, t = 0) \propto \mathrm{sinc}\left(k_c W_x \frac{x_A - x_{A'}}{2z_A}\right) \mathrm{sinc}\left(k_c W_y \frac{y_A - y_{A'}}{2z_A}\right).$$

The wavenumber k_c is the wavenumber at the carrier frequency. In a reverberating cavity, it has been shown that this enhancement factor is $\sqrt{\Delta f \tau}$.

4. NUMERICAL STUDY OF THE MODAL MODEL

The waveguide models are applied with a cylindrical waveguide of length L and radius r equal to 1 m and 5 mm, respectively. The carrier frequency is 274 GHz with a bandwidth of 2 GHz. The conductivity of aluminum is 37.7 MS/m. The horn aperture equals 10°. The horn is centered at half a radius from the center on the x-axis. The azimuth angle of the horn axis (0° azimuth corresponds to the x direction) for all incident angles is fixed to 30°. Based on Eqs. (17) and (5), we first qualitatively study the transient response between the horn antenna and the waveguide output with respect to the Tx antenna incidence. We observe in Fig. 4 that when the horn antenna axis is parallel to the waveguide one, no time dispersion is observed. Indeed, when the incident angle is smaller than the antenna angle of aperture, a part of the incident wavefront directly reaches the output. In the same plot, based on the mode group velocity, the times of arrival of all the propagating modes are plotted. For comparison, the times of arrival of the first 100 rays are also plotted. We see that only the lower modes with the fastest group velocity are excited. However, as soon as the incident angle reaches 20°, significant time dispersion is observed, and almost all the modes contribute to the transmission.

4.1. Near-Field Focusing

This angular dependence also has a strong effect on the TR focusing. Fig. 5 illustrates the spatial and temporal focusing obtained from the computation of Eq. (17) for different incident angles. When the incident angle is small, the time focusing is sharp without secondary lobes. Indeed the autocorrelation of a short pulse as seen in Fig. 4 is also a short pulse. However, because only the lower modes are excited, the spatial focusing does not occur at the right position. Indeed, a good spatial focusing requires a rich spatial diversity that is offered by a sufficiently large number of modes. Here we observe that this condition is fulfilled for angles above 40°. Note that even at 20°, the waveguide response starts to show

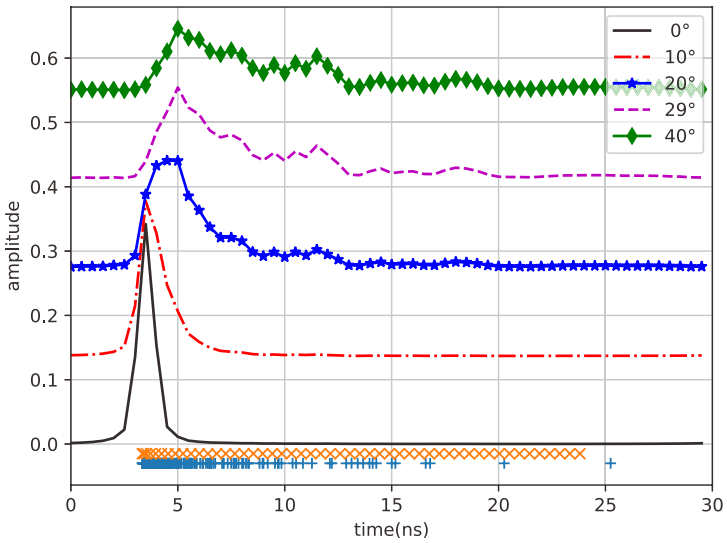

Figure 4. For each horn antenna angle, the maximum of the transmitted electric field over the waveguide output area is computed with respect to time from Eqs. (17) and (5). The markers (x) correspond to the times of arrival of the first 100 rays deduced from the image theorem (the waveguide section is assumed to be a square of the same area as the circular one). The markers (+) are deduced from the group velocities of all the propagating modes.

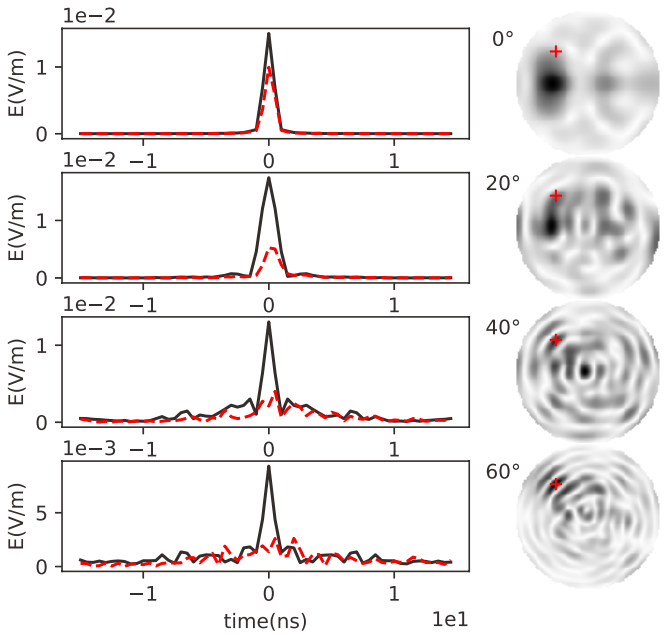

Figure 5. Spatio-temporal focusing obtained from Eq. (17) for four different horn antenna azimuth angles (0, 20°, 40° and 60°). The carrier frequency and the bandwidth equal 274 GHz and 2 GHz, respectively. On the left is plotted in a continuous black line (respect. dashed red line) the modulus of the vertically (respect. horizontally) polarized electric field at the target position, i.e., $|y(\mathbf{r}_A, \mathbf{r}_A, t)|$. On the right are shown the amplitude map of the field (vertical polarization) at the focus time and at the output of the waveguide, i.e., $|y(\mathbf{r}_A, \mathbf{r}'_A, 0)|$. The target point is shown with a red cross.

multiple paths, and the lower modes still prevail. The selective focusing effect for TR for large incident angles is also observed on the polarization. Indeed, TR focuses preferentially on the initial polarization which is vertical here.

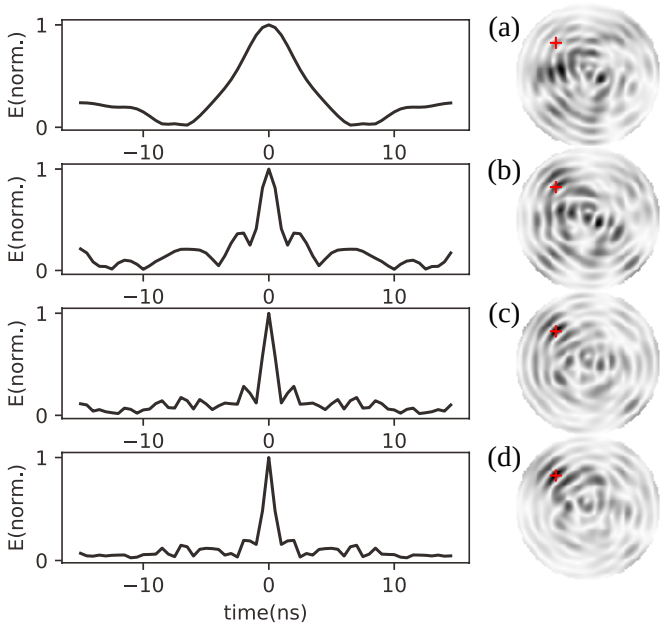

Figure 6. Spatio-temporal focusing for four different bandwidths (top to bottom) obtained from Eq. (17): (a) 500 MHz, (b) 1 GHz, (c) 1.5 GHz and (d) 2 GHz. The carrier frequency is 274 GHz. On the left is plotted the modulus of the vertically polarized electric field at the target position, i.e., $|y(\mathbf{r}_A, \mathbf{r}_A, t)|$. On the right are shown the amplitude map of the field (vertical polarization) at the focus time and at the output of the waveguide, i.e., $|y(\mathbf{r}_A, \mathbf{r}'_A, 0)|$. The target point is shown with a red cross.

We now examine the effect of the frequency bandwidth. To that end, we have plotted the spatial and temporal focusing for four different bandwidths in Fig. 6(a). As expected, the wider the bandwidth is, the shorter the focused pulse is. Indeed, the pulse width is of the order of the inverse of the bandwidth. We also observe that below a bandwidth of 1 GHz, even if the incident angle is large (60°), the maximum of field is not at the expected position. Indeed, at $t = 0$, the amplitude map is given by

$$y(\mathbf{r}_A, \mathbf{r}'_A, t) \propto \int_{-\pi\Delta f}^{\pi\Delta f} \sum_{m=0,\nu=0,n=1}^{1,\infty,\infty} \left|\left\langle \mathscr{E}^m_{\nu,n}(x,y)\right| \bar{\mathbf{E}}_B(x,y,z=0)\right\rangle\Big|^2 \times \left(\mathbf{p}^t_A \cdot \mathscr{E}^m_{\nu,n}(x_A, y_A)\right)^* \left(\mathbf{p}^t_A \cdot \mathscr{E}^m_{\nu,n}(x'_A, y'_A)\right) e^{-\alpha^m_{\nu,n} z} d\delta\omega + \text{Cross terms}. \tag{29}$$

The spatial focusing is due to the first term in Eq. (29). The second term (cross-terms) that blurs the focusing is governed by a sum that involves factors $\int e^{j(\beta^m_{\nu,n} - \beta^{m'}_{\nu',n'})} d\delta\omega$. This integral is small when $\beta^m_{\nu,n} - \beta^{m'}_{\nu',n'}$ is nonlinear, in other words, dispersive, and the integration is performed over a sufficiently wide bandwidth. The focusing improvement is confirmed when the SIR (see Table 1) is computed. The larger the bandwidth is, the larger the SIR is. With the simulation, one can also study the field enhancement. To that end, the signal to emit, either the initial pulse $e(t)$ in Eq. (1) or the response flipped in time $s^*(-t)$ in Eq. (2) is normalized by its maximum value. The enhancement factor is then

Table 1. SIR and enhancement factor with respect to the bandwidth.

Bandwidth	500 MHz	1 GHz	1.5 GHz	2 GHz
SIR (dB)	−0.9	−0.44	3.12	3.25
Enhancement factor (dB)	3.89	9.42	13.5	13.0

defined as the ratio of the maximum of the TR field, i.e., $y(\mathbf{r}_A, \mathbf{r}'_A; t)$ over the maximum of the CIR, i.e., $s(t)$. As for the SIR, we observe in Table 1 that a large bandwidth induces a high enhancement.

4.2. Far-field Beamforming

Using Eq. (21), we compute the time-reversed electric field in the far-field. Fig. 7 shows the time reversed radiation patterns to focus a field with an elevation angle of 70° and an azimuth angle of 20° (a blue arrow shows the direction). We observe that if the incident angle of the antenna is too small, a strong beam is generated in the direction of the cylinder axis. This is because the main excited mode in the waveguide is the fundamental TE11 mode that generates such a radiation pattern. However, when the incident angle is equal to 40°, a beam is generated in the expected direction. The angular resolution is linked to the cylinder radius. Based on the Airy diffraction pattern, the resolution is $1.22\lambda/2d$ where d is the diameter, in other words, 10° in this case.

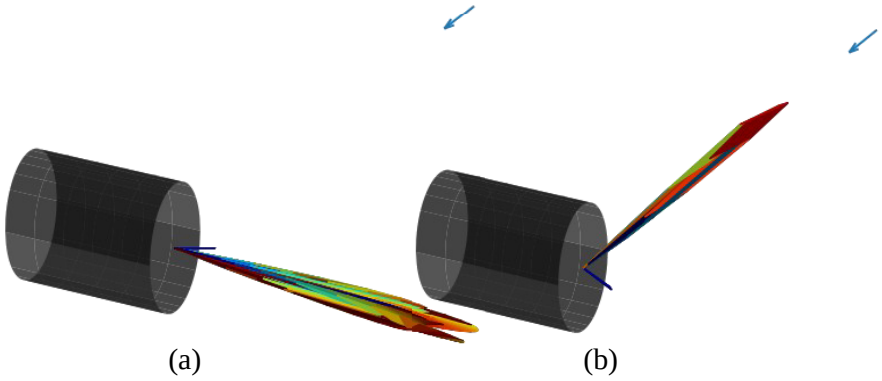

Figure 7. Far-field radiation pattern (dB scale) computed from Eq. (21) when the field is TR in the direction of the blue arrow. The carrier frequency and the bandwidth equal 274 GHz and 2 GHz, respectively. The angles of antenna A with respect to the waveguide axis are 0° and 40° for patterns (a) and (b), respectively.

5. EXPERIMENTAL RESULTS

5.1. Waveguide

The first waveguide consists of a 1-m long aluminum tube. The diameter of the cylindrical waveguide considered here equals 10 mm, in other words, about 10 times the wavelength.

The heart of the experimental setup shown in Fig. 8 is two spectrum/signal analyzer extension modules (SAXs) by Virginia Diodes, Inc. One is used to up convert an intermediate frequency (IF) signal produced by a vector signal generator (SMW200A from Rohde & Schwarz) to a carrier frequency of 273.6 GHz. This is obtained by the multiplication by a factor 48 of the frequency of a local oscillator working at 5.7 GHz. On the receiving side, the same local oscillator still multiplied by a factor 48 is used to down convert the field received by a horn antenna to an IF signal. This signal is sampled by a waveform digitizer (NI PXIe-5186). The modulation generator and waveform digitizer are synchronized by a 10 MHz reference clock. The bandwidth is limited to 2 GHz by the modulation generator. Instead of directly dealing with IF signals, for convenience, the recorded signals are numerically down-converted into in-phase and quadrature-phase pairs of signals. Each time step that lasts the inverse of the I/Q modulator bandwidth is called a tap.

We use two types of antenna provided by Virginia Diodes, Inc: a diagonal horn antenna and a dipole antenna. Their specifications are shown in Table 2. To probe the focal spot at the waveguide extremity, the dipole antenna is mounted on a linear stepper motor stage. Three CIRs are shown in Fig. 9 for three different incidence angles. For $\theta = 12°$ and $\theta = 55°$, we observe a first tap of strong

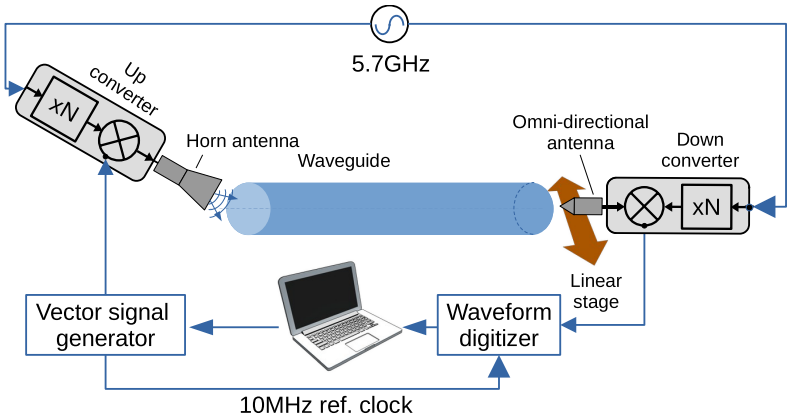

Figure 8. Experiment set-up.

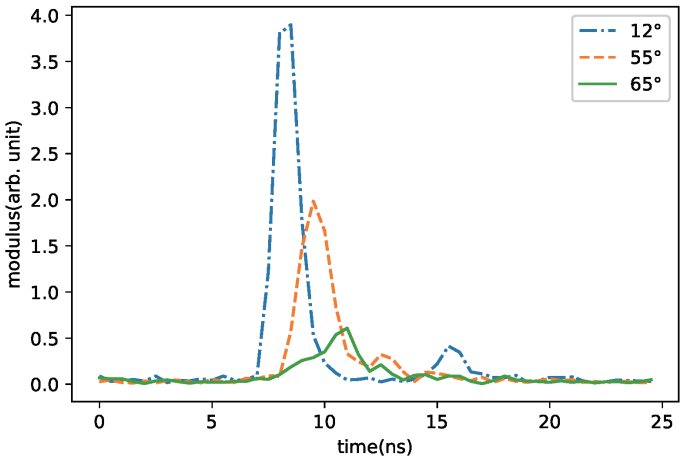

Figure 9. Experimental baseband CIR with a bandwidth of 2 GHz when the incident angle of the transmit antenna is equal to 12°, 55°, and 65°.

Table 2. Antenna specifications.

	Freq. range (GHz)	Gain (dB)	Beamwidth
Horn	260–400	26	10°
Dipole	260–400	7.5	n/a

amplitude that corresponds to the direct path. Due to the reflections, a few contributions (between 6 and 7 taps) appear for $\theta = 55°$ and $\theta = 65°$.

For $\theta = 56°$, two CIRs have been flipped in time to focus successively on two positions. Following the linear stage, the spatio-temporal focal spot has been probed on 10 different positions that are 1 mm apart. The results are shown in Fig. 10. We observe in Figs. 10(a) and (b) that the maximum is obtained at the expected position even if a strong secondary lobe seems to occur on the waveguide borders. The field enhancement may be due to the peak effect on the tube ridges. The SIRs associated with Fig. 10(a) and (b) are equal to 3 dB and 2.5 dB, respectively. For comparison, the results computed from the modal model with the same configuration are shown in Fig. 11. The best matching is obtained when the model bandwidth is equal to 1.5 GHz. We observe a qualitative agreement between the experimental and numerical results. However because of the high sensitivity of sub-THz radidations

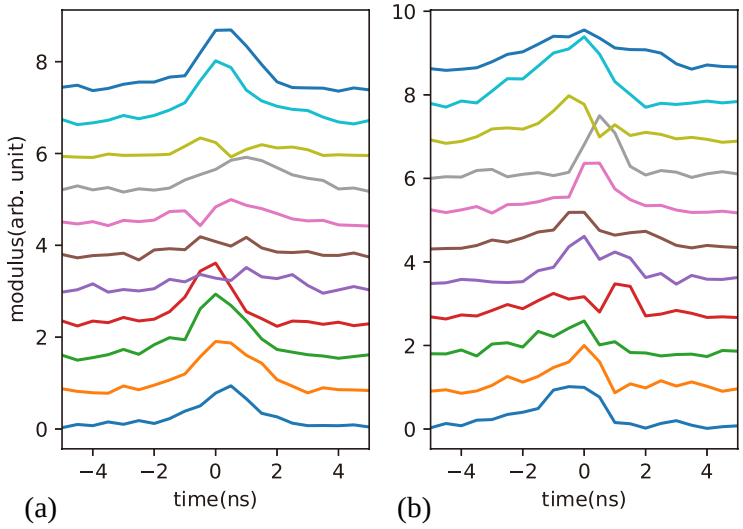

Figure 10. Experimental modulus of the baseband time-reversed signals probed at 10 positions by the omni-directional antenna when focusing on waveguide extremity at the (a) 4th and (b) 8th positions from the bottom. The probed positions are 1-mm apart. The incident angle of the horn antenna equals 56°.

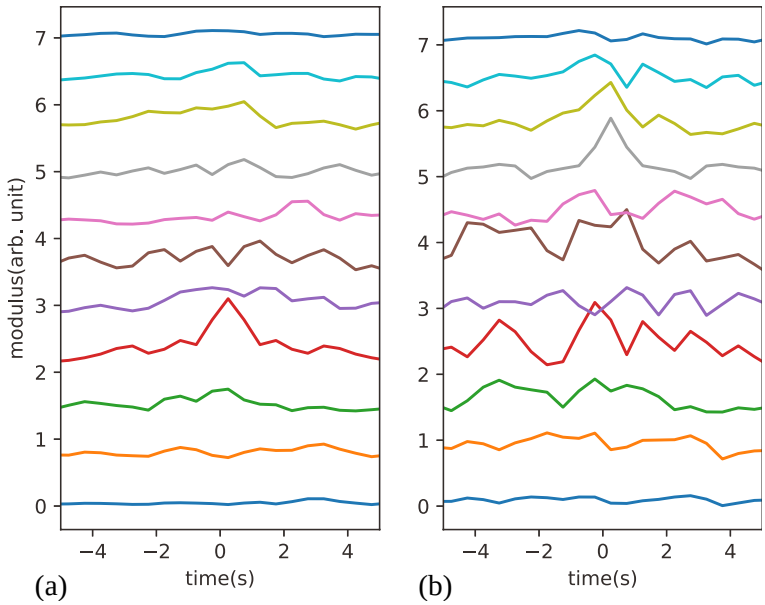

Figure 11. Modulus of the baseband time-reversed signals obtained from Eq. (17) with the same configuration as the one used to obtained Fig. 10. The bandwidth is equal to 1.5 GHz.

to many parameters (distances, radiation pattern, waveguide extremity, ...), one cannot expect the experimental and numerical waveforms to be identical.

The same TR process has been conducted but for a much smaller angle of incidence (12°) of the Tx horn antenna (see Fig. C1 in Appendix C). Instead of focusing on the correct positions, the same two spatio-temporal patterns are obtained. Therefore, the SIR is smaller (1.6 dB) for Fig. C1(a) and even negative (−2.82 dB) for Fig. C1(b). This result is consistent with Fig. 9, where, for this angle of incidence, no time dispersion is observed on the CIR. The patterns of the field appear to indicate that probably a single mode with a small amplitude at the center might be excited (such as TM01). Finally, the spatio-temporal focusing has been probed for a large angle of incidence (66°). The SIR increases to

5.4 dB and 4.5 dB (see Figs. C2(a) and (b) in Appendix C).

Before being emitted, the time-reversed CIR convoluted by the LFM is normalized by their peak value. Indeed, the maximum peak-envelope input power (PEP) of the SAX is fixed to 0 dBm. Therefore, for the three angles of incidence, the TR signal is emitted with the same maximum power. However, Figs. C1, 10, and C2 demonstrate that a larger angle of incidence leads to smaller peak amplitude. For instance, when focusing at 7 mm, the amplitude is 7 dB smaller at 55° than at 12° and even 21 dB smaller at 65°.

The effect of the bandwidth has been probed on the configuration, leading to the best SIR ($\theta = 65°$), by numerically filtering the baseband TR signal with a low-pass digital filter that preserves the phase for different cut-off frequencies. We observe in Fig. 12 that, as expected, a larger bandwidth results in a better focusing. However, for bandwidths larger than 0.5 GHz, the increase is slower. This is probably due to the Hanning window applied on the 2 GHz LFM, which reduces the effective bandwidth. Finally, contrary to the simulation results or the experiments done in acoustics or microwaves, here we do not observe an enhancement of the TR field. This is due to the convolution of the signal with LFM which prevents the benefit of the time spreading of the CIR.

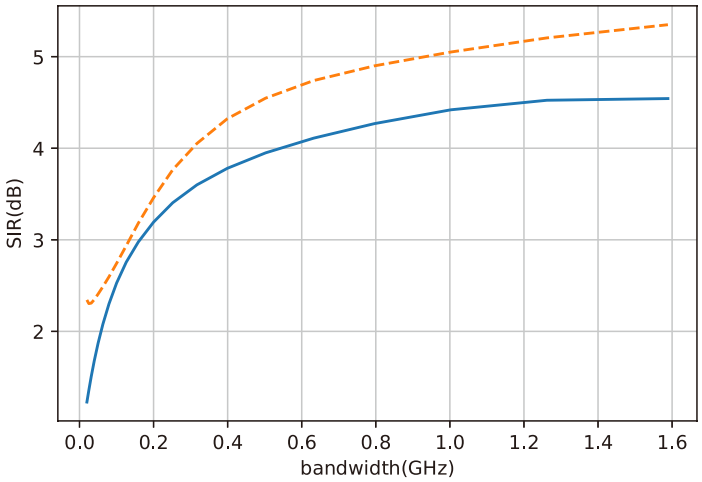

Figure 12. Signal to interference ratio with respect to the bandwidth for an angle of incidence of 65°. The continuous blue line and the dashed orange lines are obtained when focusing at the center of the waveguide and 2 mm away from the center, respectively.

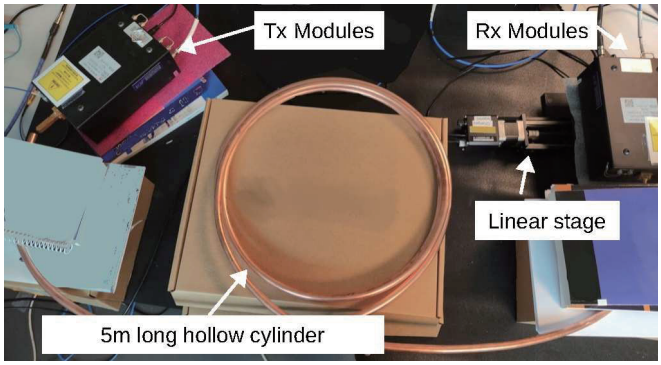

Figure 13. Illustration of the experiment performed with a 5 m long hollow cylinder waveguide.

5.2. Curved Waveguide

In principle, the longer the waveguide is, the longer the time spreading of the transient response is and the better the TR focusing is. Here it is advantageous to work with a curved waveguide which makes loops because a long and straight waveguide is difficult to handle. In this work, this configuration is only studied experimentally as the modal theory of curved waveguide is much more tedious than the straight one. Nevertheless when the radius of curvature is much larger than the inner waveguide radius, the waveguide can be considered as almost straight, and the previous conclusions would apply.

The experiment has also been performed in a 5 m long hollow cylinder (see Fig. 13). The inner diameter of the cylinder is 12 mm, and it is made of copper. The waveguide is curved and forms three superposed loops of 40 cm diameter each. The THz setup is identical to the one presented before. Unlike the shorter and straight waveguide, we do not observe direct arrival despite a relatively low angle of incidence (see Fig. D1 in Appendix D.1). After time-reversal, good quality focusing is observed (see Fig. 14). Indeed, the SIRs reach 7.3 dB and 8.2 dB when focusing at the center of the waveguide and 2 mm away from it. The focused power is similar to that obtained with a 1 m long waveguide but with an incidence angle of 66°.

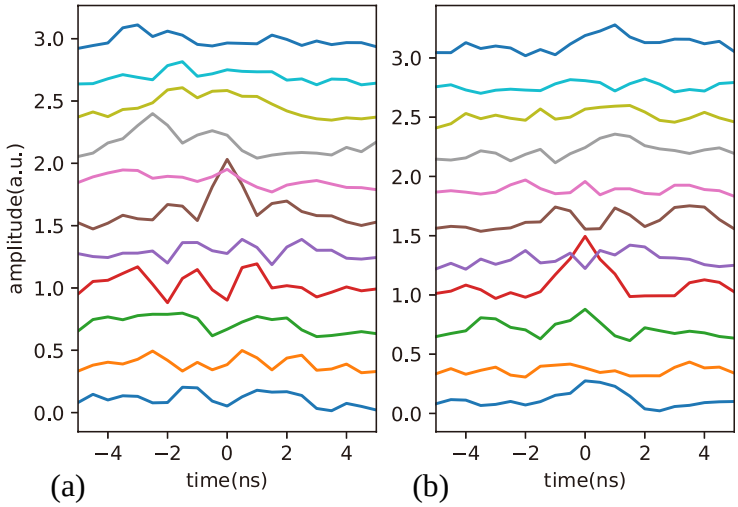

Figure 14. Modulus of the baseband time-reversed signals probed at 11 positions by the omnidirectional antenna when focusing on (a) the waveguide center and (b) 2 mm away from it, i.e., the 6th and 4th positions from the bottom. The probed positions are 1 mm apart. The incident angle of the horn antenna equals 44°.

5.3. Leaking Cavity

Soon after the pioneer works on time-reversal, it was observed that it might be very efficient to focus a wideband pulse in highly reverberating cavities. The first experiment was performed with elastic waves on a silicon wafer with a chaotic geometry [6]. A few years later, the concept was transposed to microwaves [7, 8]. Leaky cavities can be used to simultaneously benefit from the multiple reflections inside them and by remotely focusing acoustic or electromagnetic pulses [32, 33]. Here, we use the same approach as the one presented in [34] to make a cavity leak.

As shown in Fig. 15, the leaky cavity consists of a rectangular cuboid. Five of the six faces are made of aluminum, and the last one is an FR4 substrate square with a side of 52 mm. A copper grid is etched on the substrate. The width and the distance between copper strips are equal to 1 mm and 2 mm, respectively. With these dimensions, which are comparable to the wavelength, one can expect that this face acts as a semi-reflective material. A small hole allows the Tx antenna to emit inside the cavity. In this case, instead of a directional antenna, it is better to use an omnidirectional one to reach a diffuse regime more quickly, in other words, a regime where the electromagnetic field distribution is

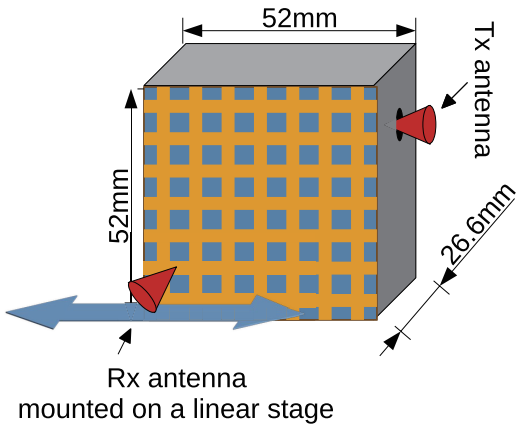

Figure 15. Leaky reverberating cavity.

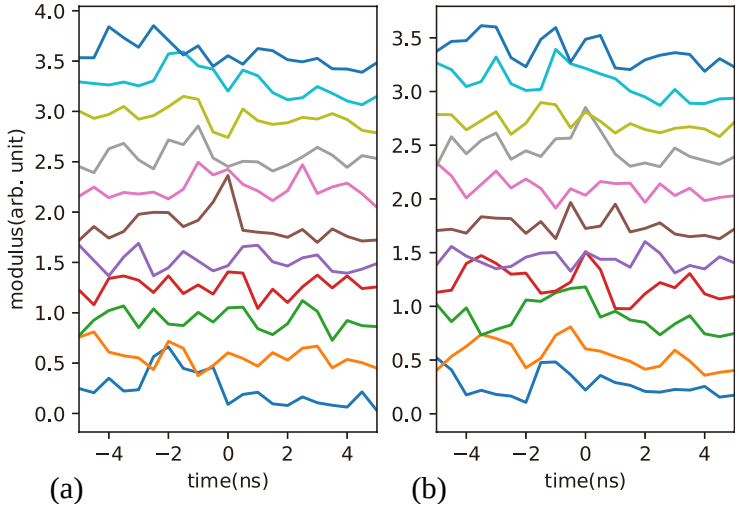

Figure 16. Modulus of the baseband time-reversed signals probed at 11 positions by the omnidirectional antenna when focusing on (a) at the center and (b) 2 mm away from it, i.e., the 6th and 8th positions from the bottom. The probed positions are 1-mm apart. The Tx antenna is inside a leaky cavity.

uniform and isotropic. The Rx omnidirectional antenna mounted on a linear motor bench is at 3.55 cm from the grid face. As the signal strength is low, ten times more averaging is required to estimate the CIR (see Fig. D2(a) in Appendix D.2). Now the decay is clearly exponential with a decay time, in other words, the time for the intensity to decrease by a factor $1/e$, of 2 ns (see Fig. D2(b) in Appendix D.2). As explained in Section 3.2, one can expect an SIR of 3 dB in our case.

However, Fig. 16 indicates that the focusing quality is not as good as expected. Indeed, the SIR when focusing on the center is 2.8 dB, but it drops to 0.9 dB when the focusing is 2 mm away. This result can be explained by an effective bandwidth that is smaller than the maximum bandwidth of 2 GHz. If we assume that the bandwidth is limited to 1.5 GHz (which is consistent with Fig. 12), the expected SIR drops to 1.8 dB, which seems more in accordance with the experiment results. Moreover, because the signal level between the Tx and Rx antenna is very small, the results shown in Fig. 16 are clearly contaminated by a significant level of noise.

6. DISCUSSION

Modern TR devices are exclusively based on digital sources and receivers. While for acoustic or even microwave applications, one can use arbitrary waveform generators and digital sampling receivers, sub-THz domain requires devices based on frequency transposition approach. This specification eliminates a wide range of sources which generates either a continuous or pulsed beam. Because not only the amplitude but also the emitted phase should be controlled, I/Q or intermediate frequency (IF) modulators/demodulators are well fitted for this application. In [35], an I/Q modulator based on a single mode-locked laser producing a stable frequency comb is presented. A modulated sub-THz signal of frequency $f_1 - f_2$ is then obtained by photomixing one comb line at f_1 with another one at frequency f_2 which is optically modulated beforehand. Here instead of an I/Q modulator, we use an IF modulator consisting of a frequency multiplier combined to a mixer and an amplifier. These devices based on Schottky-diodes belong to the family of solid state sub-THz source/receiver.

Its adaptive focusing property is very promising for sub-THz applications, such as telecommunications or imaging because it can behave, to a certain extent, as a virtual array of sub-THz antennas. Moreover due to the millimeter size of the wavelength, relatively compact devices can be developed in comparison to microwave devices. However, its application to mm-waves has some specific and restrictive features. Generally, for acoustic or microwave applications, a reverberating cavity is the best choice to benefit from the strong self-focusing property in complex media. However, we have seen that this solution is not very efficient from an energetic perspective. Indeed, only a fraction of the injected power reaches the focus, especially in lossy cavities. However, sub-mm applications usually face two major constraints: the emitted power and receiver sensitivity are simultaneously low. To overcome these limitations, this study indicates that a solution based on a waveguide is more relevant. Indeed, unlike cavities, there are no energy losses due to energy backscattered toward the source. Moreover, it is easier to control the waveguide surface state and, therefore, to limit the losses. Nevertheless, with our experimental setup, a pulse compression technique based on LFM is also required, not only to acquire the impulse response but also during the time-reversal step. In our configuration, the pulse compression was computed numerically. However, a pulse compression can also be advantageously performed with a relatively simple analog electronic circuit, which involves a voltage-controlled oscillator. The role played by time-reversal is then to address this modulated pulse to a specific location. This last property may be of interest for imaging or telecommunication applications.

7. CONCLUSION

In this paper, the time-reversal technique in the sub-THz range is evaluated experimentally for the first time, to our knowledge. It has been applied in three different complex media: a leaky and reverberating medium and in two different waveguides. We have shown that the results in the cavity are not as good as those obtained in microwaves or acoustics because of the reverberation time which is not large enough. Note that no special care has been taken to build the cavity. Perhaps, better results would be obtained in the future with a cavity where an optical-quality coating covers the inner sides. However, the best results have been obtained in the two waveguides. A semi-analytical model reproduces, at least qualitatively, the results obtained experimentally. To successfully focus the wave in the far-field or at the extremity of the waveguide, we have determined that it is important to use a directive source with a large angle of incidence. The presented results are promising for communications in 6G or THz imaging.

APPENDIX A. PEAK ENHANCEMENT

When the signals are transmitted with the same maximum amplitude arbitrarily set to 1, Eqs. (1) and (2) becomes

$$\bar{s}(t) = h_{AB}(\mathbf{r}_A, \mathbf{r}_B; t) * \frac{e(t)}{\max(|e(t)|)}, \tag{A1}$$

and

$$\bar{y}(\mathbf{r}_A, \mathbf{r}'_A; t) = \frac{e^*(-t) * h^*_{AB}(\mathbf{r}_A, \mathbf{r}_B; -t)}{\max\left(|e(-t) * h_{AB}(\mathbf{r}_A, \mathbf{r}_B; t)|\right)} * h_{BA}(\mathbf{r}_B, \mathbf{r}'_A; t), \tag{A2}$$

respectively. Assuming that $e(t)$ is the pulse of duration $1/B$ and bandwidth B, one can discretize the time such as $t \approx n/B$. The maximum of $s(t)$ is given by finding the index n that maximizes $|h_{AB}(\mathbf{r}_A, \mathbf{r}_B; n/B)/B|$, i.e., $\max_n(|h_{AB}(\mathbf{r}_A, \mathbf{r}_B; n/B)|)$. At the focus ($\mathbf{r}'_A = \mathbf{r}_A$ and $t = 0$), the amplitude of the time reversed is well approximated by

$$\bar{y}(\mathbf{r}_A, \mathbf{r}_A; t = 0) \approx \frac{1}{B} \sum\nolimits_n \frac{|h^*_{AB}(\mathbf{r}_A, \mathbf{r}_B; n/B)|^2}{\max_n(|h_{AB}(\mathbf{r}_A, \mathbf{r}_B; t)|)}, \tag{A3}$$

$$\approx \frac{\max_n(|h_{AB}(\mathbf{r}_A, \mathbf{r}_B; t)|)}{B} \tag{A4}$$

$$\times \underbrace{\sum \frac{|h^*_{AB}(\mathbf{r}_A, \mathbf{r}_B; n/B)|^2}{\max_n(|h_{AB}(\mathbf{r}_A, \mathbf{r}_B; t)|)^2}}_{>1} \tag{A5}$$

As a consequence $|\bar{y}(\mathbf{r}_A, \mathbf{r}_A; t = 0)| > |\bar{s}(t)|$.

APPENDIX B. DERIVATION OF THE AUTOCORRELATION FUNCTION

Here we derive the averaged and variance of the autocorrelation function in the case of the reverberating cavity. From the average of Eq. (25) and Eq. (24), one can easily show that

$$\langle R_{hh}(t = 0)\rangle = AB\tau. \tag{B1}$$

The average of the squared modulus of Eq. (25)

$$\left\langle |R_{hh}(t = n/B)|^2 \right\rangle = \sum_{k,k'=0}^{\infty} \left\langle a'_k a'^*_{k'} a'^*_{k-n} a'_{k'-n} \right\rangle e^{-(k+k')/B\tau} e^{n/\tau}. \tag{B2}$$

Because a_k is assumed to follow a Gaussian statistics,

$$\left\langle a'_k a'^*_{k'} a'^*_{k-n} a'_{k'-n} \right\rangle = \left\langle a'_k a'^*_{k'} \right\rangle \left\langle a'^*_{k-n} a'_{k'-n} \right\rangle + \left\langle a'_k a_{k'-n} \right\rangle \left\langle a'^*_{k'} a'^*_{k-n} \right\rangle + \left\langle a'_k a'^*_{k-n} \right\rangle \left\langle a'_{k'-n} a'^*_{k'} \right\rangle$$

if $|n| > 0$, only $\langle a_k a^*_{k'}\rangle \langle a^*_{k-n} a_{k'-n}\rangle$ is larger than 0. Therefore, it comes

$$\left\langle |R_{hh}(t = n/B)|^2 \right\rangle = A^2 \sum_{k=0}^{\infty} e^{-2k/B\tau} e^{|n|/\tau} \tag{B3}$$

$$= \frac{A^2 B\tau}{2} e^{|n|/\tau}. \tag{B4}$$

Thus, $\left\langle |R_{hh}(t = n/B)|^2 \right\rangle < \frac{A^2 B\tau}{2}$ and the SIR is given by Eq. (26).

APPENDIX C. TIME REVERSAL FOCUSING THROUGH A 1 M LONG WAVEGUIDE

The experimental setup is the one presented in Section 5.1. The only difference is the incident angle of the directional THz antenna. Fig. C1 (respectively C2) shows the results for an incidence angle of 12° (respectively 66°).

APPENDIX D. COMPLEX IMPULSE RESPONSES

D.1. 5 m Long Circular Waveguide

Figure D1 shows 11 CIRs between the sources and 11 positions just at the waveguide extremity for an angle of incidence of 44°.

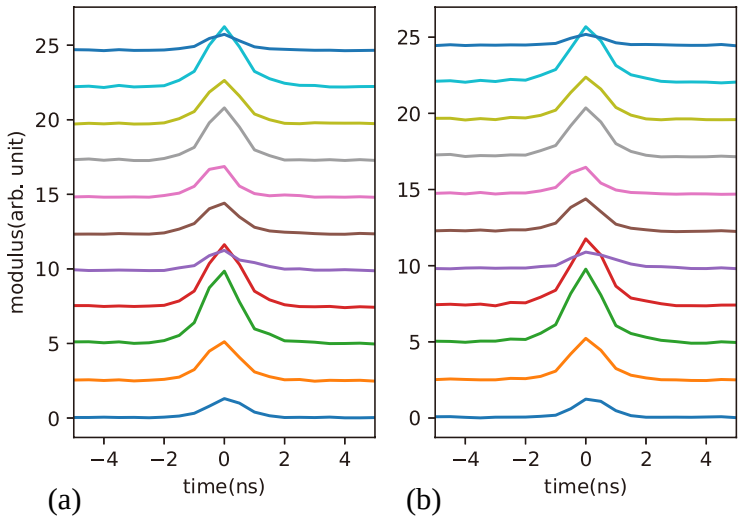

Figure C1. Modulus of the baseband time-reversed signals probed at 10 positions by the omni-directional antenna when focusing on (a) the waveguide center and (b) 2 mm away from it, i.e., the 6th and 8th positions from the bottom. The probed positions are 1 mm apart. The incident angle of the horn antenna equals 12°.

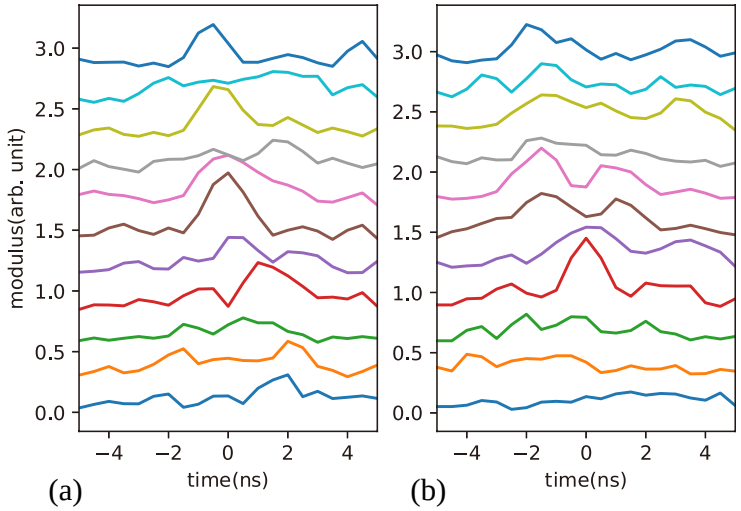

Figure C2. Modulus of the baseband time-reversed signals probed at 10 positions by the omni-directional antenna when focusing on the (a) 6th and (b) 4th positions (from the bottom). The probed positions are 1 mm apart. The incident angle of the horn antenna equals 66°.

D.2. Leaky Cavity

The aspect of the CIR shown in Fig. D2(a) is quite different from the waveguide aspects. Indeed, the field appears to decay more smoothly. This is confirmed in Fig. D2(b), where the averaged intensity over the 11 CIR is plotted. The decay is clearly exponential with a decay time, in other words, the time for the intensity to decrease by a factor $1/e$, of 2 ns. As explained in Section 3.2, one can expect an SIR of 3 dB in our case.

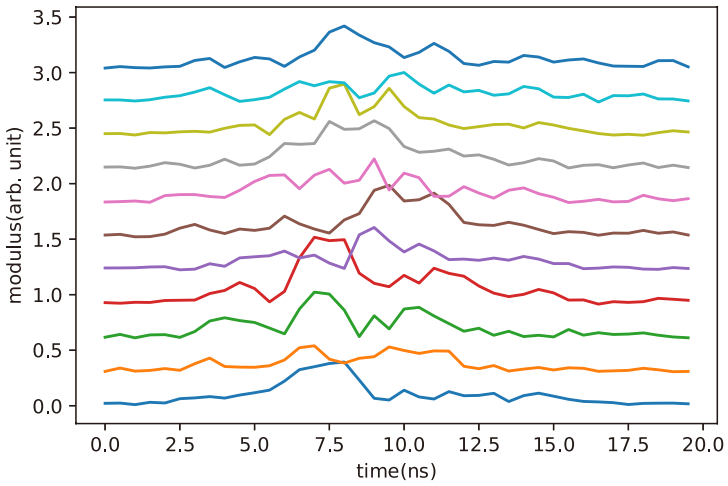

Figure D1. Eleven Baseband CIRs of a 5 m long waveguide when the incident angle of the transmit antenna is equal to 44°. The probed positions are 1 mm apart.

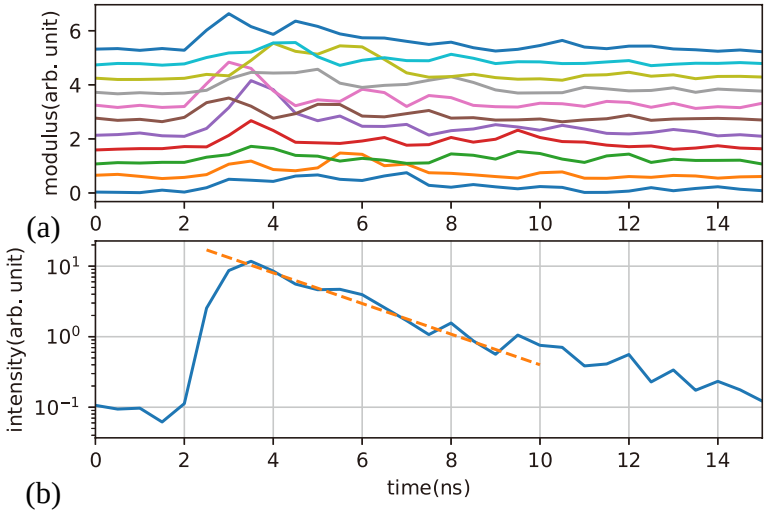

Figure D2. (a) Eleven baseband CIRs at 3.55 cm from the grid face. The probed positions are 1-mm distant. (b) Averaged intensity over the 11 positions (continuous line) and empirical linear fit (dashed line).

REFERENCES

1. Kleine-Ostmann, T. and T. Nagatsuma, "A review on terahertz communications research," *Journal of Infrared, Millimeter, and Terahertz Waves*, Vol. 32, 143, 2011.
2. Fink, M., "Time reversal of ultrasonic fields. I. Basic principles," *IEEE Transactions on Ultrasonics, Ferroelectrics, and Frequency Control*, Vol. 39, 555, 1992.
3. Wu, F., J.-L. Thomas, and M. Fink, "Time reversal of ultrasonic fields. Il. Experimental results," *IEEE Transactions on Ultrasonics, Ferroelectrics and Frequency Control*, Vol. 39, 567, 1992.
4. Derode, A., P. Roux, and M. Fink, "Robust acoustic time reversal with high-order multiple scattering," *Physical Review Letters*, Vol. 75, 4206, 1995.
5. Roux, P. and M. Fink, "Time-reversal in a waveguide," *The Journal of the Acoustical Society of America*, Vol. 110, 2631, 2001.

6. Draeger, C. and M. Fink, "One-channel time reversal of elastic waves in a chaotic 2D-silicon cavity," *Physical Review Letters*, Vol. 79, 407, 1997.
7. Lerosey, G., J. De Rosny, A. Tourin, A. Derode, G. Montaldo, and M. Fink, "Time reversal of electromagnetic waves," *Physical Review Letters*, Vol. 92, 193904, 2004.
8. Lerosey, G., J. De Rosny, A. Tourin, A. Derode, and M. Fink, "Time reversal of wideband microwaves," *Applied Physics Letters*, Vol. 88, 154101, 2006.
9. Edelmann, G. F., T. Akal, W. S. Hodgkiss, S. Kim, W. A. Kuperman, and H. C. Song, "An initial demonstration of underwater acoustic communication using time reversal," *IEEE Journal of Oceanic Engineering*, Vol. 27, 602, 2002.
10. Hengy, S., P. Hamery, S. De Mezzo, and P. Duffner, "Networked localization of sniper shots using acoustics," *SPIE Defense, Security, and Sensing*, 804602–804602, International Society for Optics and Photonics, 2011.
11. Pernot, M., J.-F. Aubry, M. Tanter, A.-L. Boch, F. Marquet, M. Kujas, D. Seilhean, and M. Fink, "In vivo transcranial brain surgery with an ultrasonic time reversal mirror," *Journal of Neurosurgery*, Vol. 106, 1061, 2007.
12. Thomas, J.-L., F. Wu, and M. Fink, "Time reversal focusing applied to lithotripsy," *Ultrasonic Imaging*, Vol. 18, 106, 1996.
13. Chakroun, N., M. Fink, and F. Wu, "Time reversal processing in ultrasonic nondestructive testing," *IEEE Transactions on Ultrasonics, Ferroelectrics and Frequency Control*, Vol. 42, 1087, 1995.
14. Wang, C. H., J. T. Rose, and F.-K. Chang, "A synthetic time-reversal imaging method for structural health monitoring," *Smart Materials and Structures*, Vol. 13, 415, 2004.
15. Roux, P., A. Derode, A. Peyre, A. Tourin, and M. Fink, "Acoustical imaging through a multiple scattering medium using a time-reversal mirror," *The Journal of the Acoustical Society of America*, Vol. 107, L7, 2000.
16. Wang, M., G. Yang, W. Li, and Q. Wu, "An overview of cancer treatment by terahertz radiation," *2013 IEEE MTT-S International Microwave Workshop Series on RF and Wireless Technologies for Biomedical and Healthcare Applications (IMWS-BIO)*, IEEE, 2013.
17. Echchgadda, I., J. E. Grundt, C. Z. Cerna, C. C. Roth, J. A. Payne, B. L. Ibey, and G. J. Wilmink, "Terahertz radiation: A non-contact tool for the selective stimulation of biological responses in human cells," *IEEE Transactions on Terahertz Science and Technology*, Vol. 6, 54, 2016.
18. Cooper, K. B., R. J. Dengler, N. Llombart, B. Thomas, G. Chattopadhyay, and P. H. Siegel, "THz imaging radar for standoff personnel screening," *IEEE Transactions on Terahertz Science and Technology*, Vol. 1, 169, 2011.
19. Wietzker, S., C. Jördens, N. Krumbholz, B. Baudrit, M. Bastian, and M. Koch, "Terahertz imaging: A new non-destructive technique for the quality control of plastic weld joints," *Journal of the European Optical Society: Rapid Publications*, Vol. 2, 2007.
20. Song, H.-J. and T. Nagatsuma, "Present and future of terahertz communications," *IEEE Transactions on Terahertz Science and Technology*, Vol. 1, 256, 2011.
21. Zhang, Y., W. Zhou, X. Wang, Y. Cui, and W. Sun, "Terahertz digital holography," *Strain*, Vol. 44, 380, 2008.
22. Ruffin, A. B., J. Decker, L. Sanchez-Palencia, L. L. Hors, J. F. Whitaker, T. B. Norris, and J. V. Rudd, "Time reversal and object reconstruction with single-cycle pulses," *Optics Letters*, Vol. 26, 681, 2001.
23. Ruffin, A. B., J. V. Rudd, J. Decker, L. Sanchez-Palencia, L. L. Hors, J. F. Whitaker, and T. B. Norris, "Time reversal terahertz imaging," *IEEE Journal of Quantum Electronics*, Vol. 38, 1110, 2002.
24. Buma, T. and T. B. Norris, "Time reversal three-dimensional imaging using single-cycle terahertz pulses," *Applied Physics Letters*, Vol. 84, 2196, 2004.
25. Lopato, P. and T. Chady, "Time reversal pulsed terahertz inspection of dielectric structures," *International Journal of Applied Electromagnetics and Mechanics*, Vol. 39, 427, 2012.

26. Musheinesh, M. A., C. J. Divin, J. A. Fessler, and T. B. Norris, "Time-reversal and model-based imaging in a THz waveguide," *Optics Express*, Vol. 17, 13663, 2009.
27. Draeger, C. and M. Fink, "One-channel time-reversal in chaotic cavities: Theoretical limits," *The Journal of the Acoustical Society of America*, Vol. 105, 611, 1999.
28. Draeger, C., J.-C. Aime, and M. Fink, "One-channel time-reversal in chaotic cavities: Experimental results," *The Journal of the Acoustical Society of America*, Vol. 105, 618, 1999.
29. Derode, A., A. Tourin, and M. Fink, "Ultrasonic pulse compression with one-bit time reversal through multiple scattering," *Journal of Applied Physics*, Vol. 85, 6343, 1999.
30. Borcea, L., G. Papanicolaou, C. Tsogka, and J. Berryman, "Imaging and time reversal in random media," *Inverse Problems*, Vol. 18, 1247, 2002.
31. Goodman, J., *Statistical Optics*, Wiley, New York, 2000, ISBN 9780471399162.
32. Montaldo, G., P. Roux, A. Derode, C. Negreira, and M. Fink, "Ultrasound shock wave generator with one-bit time reversal in a dispersive medium, application to lithotripsy," *Applied Physics Letters*, Vol. 80, 897, 2002.
33. Davy, M., J. de Rosny, J.-C. Joly, and M. Fink, "Focusing and amplification of electromagnetic waves by time reversal in an leaky reverberation chamber," *Comptes Rendus Physique*, Vol. 11, 37, 2010.
34. Dupré, M., M. Fink, and G. Lerosey, "Using subwavelength diffraction gratings to design open electromagnetic cavities," *Physical Review Letters*, Vol. 112, 043902, 2014.
35. Koenig, S., D. Lopez-Diaz, J. Antes, F. Boes, R. Henneberger, A. Leuther, A. Tessmann, R. Schmogrow, D. Hillerkuss, R. Palmer, et al., "Wireless sub-THz communication system with high data rate," *Nature Photonics*, Vol. 7, 977, 2013.